

A Quick-and-Dirty Method for Assessing the Risk of Negative Aeration Effects of Shock Absorbers Equipped with Shim Sliding Base Valves

Piotr CZOP¹⁾*, Jacek GNIŁKA²⁾

¹⁾ *AGH University of Science and Technology, Kraków, Poland*

²⁾ *Institute of Theoretical and Applied Mechanics, Silesian University of Technology, Gliwice, Poland*

* *Corresponding Author e-mail: pczop@agh.edu.pl*

This paper presents a quick-and-dirty method to assess the risk of negative aeration effects occurring in twin-tube hydraulic shock absorbers used in passenger cars at the early design stage. The method is intended to be implemented as an engineering calculation tool based on the computational fluid dynamics (CFD) two-dimensional (2D)/three-dimensional (3D) steady-state single-phase model. The CFD model was previously validated with the use of the particle image velocimetry (PIV) experiment. The negative aeration effect is a well-known issue for automotive and railway shock absorbers manufacturers. It results in uncontrolled on-vehicle vibrations and the deteriorated shock absorber damping characteristic. The major aeration contributor in twin-tube hydraulic shock absorbers is the sliding shim intake valve, which requires design optimization to avoid a negative aeration effect. The method validation was conducted with the customized test rig equipped with a transparent cylinder where the specific sliding intake valve was assembled. The proposed method also requires a lumped-parameter model of a twin-tube shock absorber, which allows to simulate boundary conditions in assessing particular reservoirs of a shock absorber, i.e., pressures and flow balance. The method is implemented as a calculation routine that converts CFD pressure regions into a gas concentration indicator (GCI) using the pressure-density characteristic of an oil-gas emulsion of a shock absorber. GCI is calculated based on the sum of particular 2D/3D grid elements. The method application is to minimize the risk of occurrence of negative aeration effects by avoiding expensive and time-consuming experimental tests. This method can also be used for in-production shock absorbers projects as a part of a continuous improvement cycle or in the case of inefficient shock absorbers claimed by a vehicle manufacturer. The application scope of the method can be extended for arbitrary twin-tube designs of shock absorbers in the automotive and railway industries.

Keywords: twin-tube, passenger car, shock absorber, PIV, CFD, quick-and-dirty, optical measurements, vibrations, simulation model, aeration effect, sliding intake valve, shim-relief valve.



ABBREVIATIONS

- CFD – computational fluid dynamics,
 DES – detached eddy simulation mathematical turbulence model,
 DOE – design of experiment,
 FEA – finite element analysis,
 FEM – finite element method,
 FSI – fluid structure interaction,
 GCI – gas concentration indicator,
 LES – large eddy simulation mathematical turbulence model,
 PIV – particle image velocimetry
 RANS – Reynolds-averaged Navier–Stokes mathematical turbulence model,
 RSM – Reynolds stress model,
 SAS – scale adaptive simulation,
 SST – shear-stress transport.

NOTATION

- A_e – aeration number [–],
 Ca – cavitation number [–],
 i – discrete finite element [–],
 $f_{\text{CFD}}(\cdot)$ – function conducting CFD simulation [–],
 $f_{\text{GCI}}(\cdot)$ – function obtaining gas concentration indicator (GCI) [–],
 m_{oil} – oil mass [kg],
 m_{gas} – mass of the free and the dissolved gas [kg],
 m_{emulsion} – mass of the gas and the oil [kg],
 p_p – partial pressure of the gas over the liquid surface in the reservoir in the steady conditions in the liquid saturated state [Pa],
 p_{ini} – initial pressure in the container [Pa],
 p_0 – atmospheric pressure corresponding to the pressure during the storage of the liquid,
 p_G – partial pressure of the gas above the oil-gas emulsion [Pa],
 m_{ini} – initial mass of gas dissolved in given oil volume (hydraulic reservoir) [kg],
 p_G^{ini} – initial pressure of the pressurizing medium [Pa],
 \mathbf{v} – matrix of velocities [m/s],
 \mathbf{p} – matrix of pressures [Pa],
 \mathbf{m}_{gas} – matrix of the free and the dissolved gas mass values [kg],
 $\mathbf{m}_{\text{fluid}}$ – matrix of fluid mass values [kg],
 V_{gas} – gas chamber volume [m³],
 V_{oil} – total oil volume [m³],
 V_l – liquid volume [m³],
 x, y, z – Cartesian coordinates [m],
 t – continuous time [s],
 α_v – the so-called Bunsen solvability coefficient [–],
 η – gas concentration indicator (GCI) [–],
 χ – experimental aeration measure [–],
 v – elocity [m/s],
 ρ – density [kg/m³],

- ρ_{fluid} – density of oil [kg/m³],
- ρ_{gas} – density of gas [kg/m³],
- ρ_{emu} – density of oil and gas emulsion [kg/m³].

1. INTRODUCTION

An important contributor to the low- and high-frequency ride performance of a twin-tube shock absorber widely used in the automotive and railway industries is the occurrence of either the aeration or the cavitation (or both) phenomena. A twin-tube shock absorber is a hydraulic device composed of a set of control valves and reservoirs in which the fluid is in direct contact with the gas and such fluid is forced to flow through the fixed and variable restrictions of valves [13]. Cavitation and aeration are caused by hydraulic restrictions where potential fluid pressure energy is converted to kinetic energy, increasing the fluid flow velocity and locally reducing the pressure. Nevertheless, the aeration effect occurs more frequently and is much more common than the cavitation effect [13]. The joint effect of aeration and cavitation causes a delay while building up the pressure difference across the valve, resulting in hysteresis on the valve characteristic curve. It affects the operational shock absorber performance through damping characteristic deterioration and the existence of a hysteresis loop in the force-velocity response [13, 15]. In other words, in hydraulic shock absorbers, the presence of entrained gas or vapor bubbles results in a large piston displacement before a significant pressure drop across the piston is built. Those negative effects are all attributable to significantly increased fluid compressibility caused by the existence of either gas (aeration) or liquid vapor phase (cavitation). Therefore, the automotive and railway vehicle suspension engineering design process requires a quick-and-dirty method as an analytical prediction tool to immediately indicate the risk of aeration/cavitation occurrence at the early shock absorber design stage. In this respect, the authors proposed to develop a single phase steady-state CFD model combined with the lumped twin-tube shock absorber model developed and validated it in previous applications [7]. The model allows to obtain macro-level hydraulic parameters, e.g., the mass flow balance and pressures in shock absorber reservoirs. The authors aim to tackle a research problem: formulate a CFD model and validate it using a dedicated PIV experiment. The authors contribute also by designing the patented fixture allowing PIV measurements under the semi-operation of a shock absorber [9].

The content of the paper is divided into nine sections. Section 2 presents a brief simulation and experimental study addressing the negative effect of aeration, while Sec. 3 provides a literature review for aeration and cavitation occurrence conditions. Section 4 introduces the aeration risk assessment method. Sections 5 and 6 discuss a CFD simulation model and a PIV measurement ex-

perimental setup, respectively. Section 7 shows the validation results of the CFD model vs. PIV measurements, while Sec. 8 shows how the method was applied to evaluate the risk of aeration. Finally, Sec. 9 presents the summary of the paper.

2. PROBLEM DEMONSTRATION

In shock absorber reservoirs, there is an interface surface between the working medium of the hydraulic device and the gas being the pressurizing medium. The gas pressure allows an amount of the gas to dissolve in the hydraulic medium. Valve design geometry and parameters affect the fluid flow while passing through the valve interior. A brief simulation and experimental study are demonstrated hereafter to show the severity and importance of activities leading to minimizing negative aeration effects. The ratio of the gaseous mass fraction m_{gas} (the mass of the free and the dissolved gas) to the total mass of the oil (the emulsion) contained in the twin-tube shock absorber [13] is defined as the parameter χ :

$$\chi = \frac{m_{\text{gas}}}{m_{\text{emulsion}}} = 1 - \frac{m_{\text{oil}}}{m_{\text{gas}} + m_{\text{oil}}}. \quad (1)$$

The negative aeration and cavitation effects can be simulated using the lamped-parameter twin-tube shock absorber model [7]. The simulation was conducted with two values of χ : $\chi = 1\text{E-}08$ and $\chi = 1\text{E-}05$. The shock absorber model was excited using a sine waveform of a stroke of 80 mm, frequency of 4 Hz, and velocity of 0.3 m/s.

The low-frequency (0–20 Hz) negative effects of aeration are the lower dissipating energy, delay in the build-up of damping force (Fig. 1a) or, equivalently, slower than expected increase of pressure in the chambers, and the hysteresis loop in the force-velocity response (Fig. 1b) attributable to abnormal fluid compressibility, which is caused by the existence of either gas (aeration) or liquid vapor phase (cavitation) at certain stages of the stroking cycle.

The high-frequency (20–1000 Hz) negative effects, manifesting themselves as excessive vibrations (Fig. 1c) and emission of noise [13], are caused by an abrupt and catastrophic collapse of cavities entrapped in the hydraulic liquid, and are attributed to the aeration and cavitation phenomena as well [2].

The negative aeration and cavitation effects can also be reproduced during experimental tests with the use of a twin-tube transparent shock absorber. Two measurements in a sequence were performed in order to obtain the parameter χ . The transparent twin-tube shock absorber used in the test (Fig. 2) is equipped with an external tube made of transparent material to enable measuring the volume of working medium emulsion. The parameter χ is calculated knowing the mass balance of the working fluid medium and the height of the oil column in the transparent reservoir. The analytical formula is given further in the paper

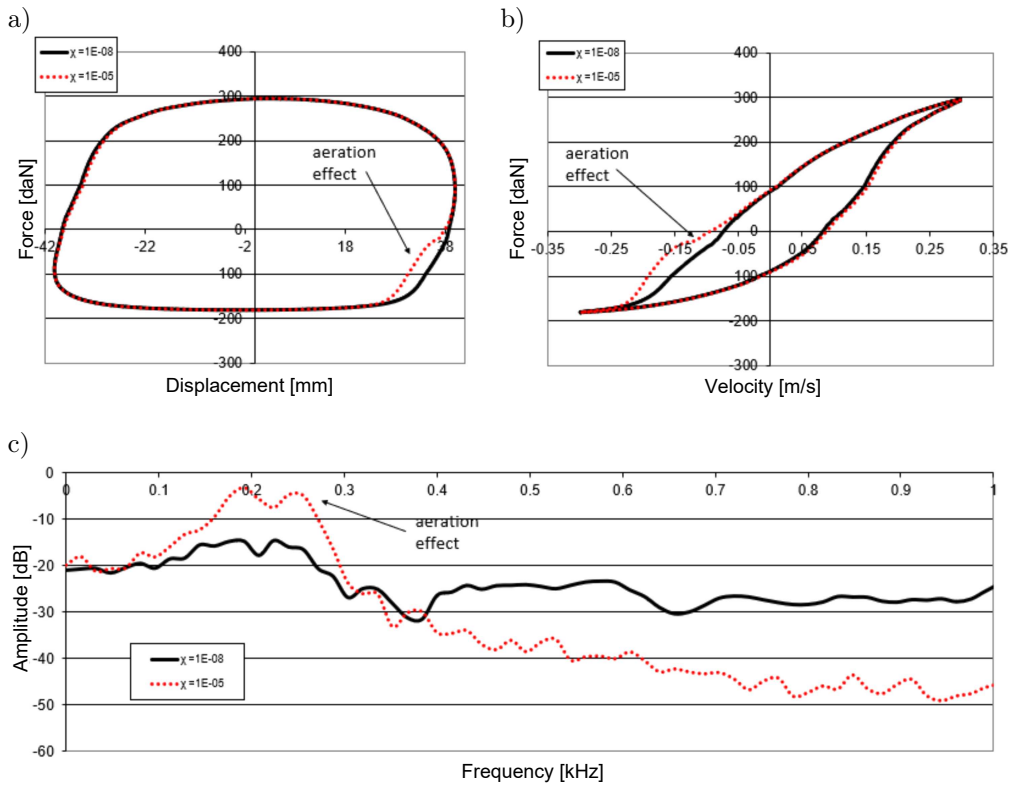


FIG. 1. Dynamic shock absorber characterization using: a) damping-displacement characteristic, b) damping-velocity characteristic, c) power spectrum vibration characteristic obtained for two values of the χ parameter: normal $1E-08$ and high value $1E-05$.



FIG. 2. A transparent shock absorber installed in the test rig.

with Eqs. (8) and (9) and corresponding descriptions in the text. It is observed that obtained value of the parameter χ is a function of the number of testing cycles and the same is the function of oil temperature.

Figure 3 shows an evolution of the χ parameter during both tests.

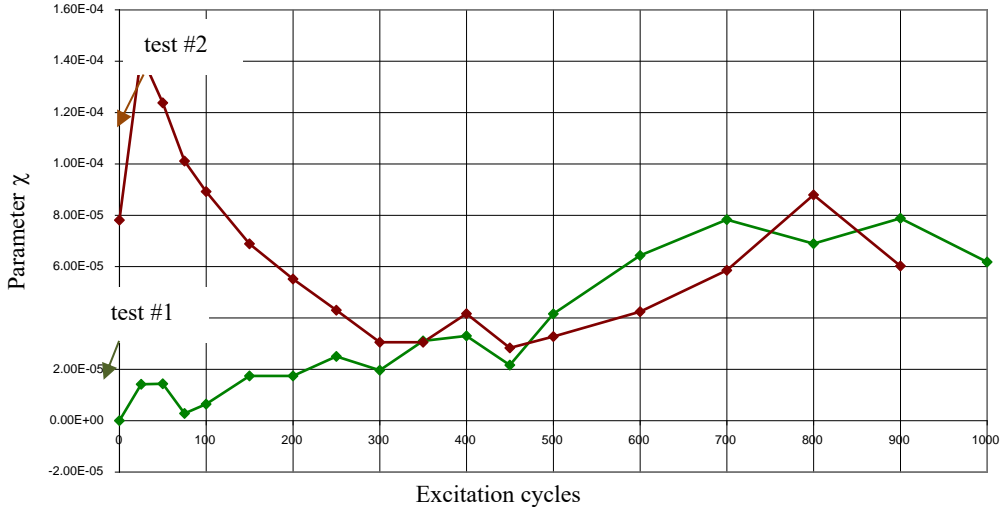


FIG. 3. Evolution of the average value of the parameter χ as a function of the number of shock absorber cycles (sinewave, stroke 80 mm, frequency 4 Hz, velocity 0.3 m/s).

The green line depicts a trend of the parameter χ for the first part of the test (test #1), i.e., the test with freshly refilled oil, while the brown line presents a trend of the parameter χ for the second part of the test (test #2), i.e., the test continuation after approximately 2 hours of cooling the unit down without changing the oil.

Restoration of the initial parameter χ is achieved by either the gas re-absorption to the working medium or condensation of liquid vapor back to the form of the liquid (see [33] and [8]). Nevertheless, other internal and external factors may affect shock absorber operation, e.g., oil type, excitation stroke amplitude, frequency and velocity, and shock absorber housing properties by means of heat accumulation and dissipation (mono-tube, twin-tube, other designs). It is usually required to maintain the shock absorber with no movements in a vertical position for 2–3 days to release most of the aeration bubbles to recover the initial oil conditions.

3. LITERATURE REVIEW

The cavitation phenomenon occurs when oil ruptures under the influence of tensile stress, which manifests itself as a number of very small cavities in the

oil [9]. The process of cavitation depends, among others, on the purity of the liquid and the rate at which the liquid is stressed [15]. In other words, cavitation is the formation of pockets of vapor in a liquid, which occurs when the local ambient pressure at a point in the liquid falls below the liquid's vapor pressure, and the liquid undergoes a phase change to a gas, creating "bubbles" or, more accurately, cavities in the liquid. The lifespan of a typical cavitation bubble is very short as it tends to collapse immediately after its occurrence. Violent (catastrophic) collapses of cavitation or aeration bubbles result in the emission of noise as well as material damage to nearby solid surfaces [9]. Noise is a consequence of the large pressure (shock) wave generated during bubble implosion, which is also responsible for the occurrence of a micro-flow in the liquid [8]. The cavitation risk rises when the pressure in the rebound chamber during the compression stroke becomes lower than the vapor pressure of the damper oil (~ 0 MPa). This results in a damping force lag during the start of the next rebound stroke since the voids must collapse first. If, during a compression stroke, the pressure in the upper-pressure tube chamber becomes lower than the pressure in the reserve tube chamber, gas (nitrogen) from the reserve tube is sucked into the pressure tube through the rod-guide seal, which also results in a damping force lag during the start of the next rebound stroke.

The aeration phenomenon in a twin-tube shock absorber is defined as a process by which gas, typically nitrogen, is circulated through, mixed with, or dissolved in oil being used as a working fluid in shock absorbers. Gas is included in shock absorbers under certain pressure, separately from the oil, to provide compressibility to allow for the rod displacement volume compensation. Theory states [1] that a liquid exposed to a soluble gas (i.e., the liquid coming into contact with the atmosphere of a gas that can dissolve in it) is in one of three forms: liquid-gas solution, liquid-gas bubble emulsion or foam. The liquid-gas solution is prone to bubble formation when the pressure of the liquid-gas solution falls below the so-called saturation pressure. In this state, the liquid can no longer retain all the gas in its dissolved form, and therefore, bubbles occur. The solubility of gas in a liquid is directly proportional to the absolute pressure above the liquid surface (Henry's law), and normally decreases with rising temperature [1]. All of the mentioned liquid-gas mixtures can be considered as liquid with pockets of gas or vapor. The dissolved gas has a significant influence on the oil mixture and thus on the shock absorber's behavior. The presence of gas bubbles is the cause of the damping force loss in the shock absorber. It is an undesirable and negative effect visible as asymmetry of the force displacement characteristic and should be minimized. Modeling the dynamics of gas bubble formation and transport is a task that is very difficult for several reasons. The most important ones are the difference between the time scales in which aeration processes occur (order of minutes) and the time scales of oil flow through

a damper (order of seconds), the existence of uncontrollable parameters on which bubble size depends, and the bubble itself (e.g., oil impurities and sharp edges), as well as the re-absorption of gas from bubble surfaces, etc. The aeration risk rises when the oil temperature in a shock absorber increases due to severe operation, e.g., off-road driving and bumpy-road driving. In turn, the oil viscosity decreases, reducing the damping force effectiveness of valve systems and shock absorbers. The risk is greater if the nitrogen gas is not separated from the oil, as it is in mono-tube shock absorbers.

Among others, the research engineering team of which the authors were members, developed in 2005–2018 theoretical and experimental methods suitable for evaluation of shock absorbers cavitation and aeration effect, which found use in engineering applications. The authors' contribution, introduced in this paper, is novel in the sense of an applied research approach to solve a specific design problem of twin-tube shock absorbers.

Czop and Gniłka [5] used the fluid structure interaction (FSI) model in order to quantify the aeration and cavitation phenomena by means of the finite element method (FEM) simulation. Czop *et al.* [8] used a lumped parameter model to minimize damping lag in hydraulic twin-tube shock absorbers. The analytical and theoretical studies conducted by the authors and the research team were also accompanied by many experimental tests and investigations. A novel experimental method to evaluate the combined effect of aeration and cavitation on hydraulic shock absorber damping was formulated by Włodarczyk *et al.* [33]. Design of experiment (DOE) method for assessing the risk of negative aeration was used by Czop *et al.* [10] and Sławik *et al.* [30] to calculate the experimental measure, which was further correlated with a theoretical gas concentration measure. The particle image velocimetry (PIV) technique [3, 12, 27, 29, 32] was used by several authors to correlate the CFD model with experimental results. Czop *et al.* [6] presented the measurement procedure with the granted patent for an experimental setup [9].

Other researchers developed the foundations for the presented quick-and-dirty method and its engineering application. Duym *et al.* [15] developed a lumped parameter model of a shock absorber and aeration-cavitation effect visualization technique along model correlation method. Dixon [13] provided a general engineering-based discussion. Alonso and Comas [1] introduced lumped-parameter model well correlated with experimental observations. Herr *et al.* [35] proposed a combined mathematical model of a twin-tube shock absorber that included component models developed using CFD techniques. The component CFD analysis allowed to investigate the unique features of flow pattern, discharge coefficient, and pressure distribution inside the shock absorber components, i.e., valve systems and a rod-guide. Luo and Zhang [22] provided a comprehensive review of lumped-parameter modeling methods for aeration and cavitation phe-

nomena. Andrighetto [11] developed the complementary dynamical and thermal model of a shock absorber. Morettini *et al.* [24] conducted experimental investigations, while Koren *et al.* [18] focused on predicting a high-frequency oil-flow phenomena in hydraulic shock absorbers. The inspiration and helpful information were also found in Iyer and Yang [16] who presented a relevant analytical study on the dynamics and hydrodynamic stability of liquid-vapor mixtures in the bubble-flow range in reciprocating motion through a horizontal channel applicable to the optimization of shock absorber development. Martins *et al.* [29] analyzed 2D contour flow characteristics based on the CFD model of a shim valve system. Koren *et al.* [18] discussed the method for prediction high-frequency oil-flow phenomena in hydraulic shock absorbers using 2D unsteady Euler equations. Shams *et al.* [36] used coupled CFD and finite element analysis (FEA) approach to predict the damping force of the piston valve used in an automotive twin-tube shock absorber. The simulation results were also successfully verified experimentally. Kulkarni *et al.* [37] demonstrated the application of the FSI method to the shim valve's modeling, including experimental validation results. Guzzomi *et al.* [38] presented a two-way FSI approach for the prediction of a valve system performance by coupling the valve shim stack deflection FE model with the fluid flow CFD model. That study applied a similar methodology as proposed in this paper which was used for the prediction of valve fluid-flow characteristics.

4. THE METHOD TO EVALUATE THE AERATION RISK

An intended method is a quick-and-dirty approach aiming at optimizing and preselecting the most promising shock absorber configurations. The method is efficient enough to verify two–three shock absorber configurations in an hour. The engineering skills and flexibility cannot be replaced by the proposed method; however, the method standardizes the design workflow and works as an applied quality standard and early warning in the case of incorrect shock absorber design. The method is based on a heuristic assumption that properties of the fluid in motion may be derived from steady-state simulations by applying certain data processing algorithms before being converted into the valve design ranking parameter. This proposition is asymptotically valid under the assumption that the flow in all the chambers is strongly mixing. Discussion of mixing types is beyond the scope of this text; thus, the interested reader is referred to [20] and references therein. Finally, the developed method of aeration risk assessment requires the following assumptions:

- only an aeration phenomenon is present in a twin-tube shock absorber neglecting the cavitation effect,

- the gas bubbles are small so that their compression is isothermal (isothermal compression may be assumed for small bubbles and adiabatic compression for large gas pockets),
- a major contributor to a shock absorber deterioration regarding negative aeration effect is the base valve (it is usually a sliding type of the valve),
- lumped parameter twin-tube shock absorber model is required to be previously validated based on experimental results in order to obtain mass flow balance and pressures in shock absorber reservoirs, particularly differential pressures across the base valve assembled in the inner cylinder-end of a twin-tube shock absorber [7],
- distributed-parameter CFD model should be parameterized,
- CFD model should be previously calibrated and validated based on the representative cases using the PIV experimental technique,
- analytical finite element volume cell counting technique is used to indicate the risk of aeration.

The phenomenon of cavitation discussed in Sec. 3 is characterized by the dimensionless number, the so-called cavitation number [13]:

$$\text{Ca} = 2 \cdot \frac{p - p_v}{\rho v^2}, \quad (2)$$

where p_v is the vapor pressure of the liquid of density ρ flowing with the characteristic velocity v , and $p = p(x, y, z; t)$ is the local pressure in the flow. The presence of the factor of 2 in Eq. (2) results from the mathematical simplification of the energy term in the denominator. By analogy, the phenomenon of aeration is characterized by the aeration number:

$$\text{Ae} = 2 \cdot \frac{p - p_p}{\rho v^2}, \quad (3)$$

where p_p is the partial pressure of the gas over the liquid surface in the reservoir in the steady conditions in the liquid saturated state. Density term in Eqs. (2) and (3) refers to the fluid density before the effect development – in the sense that these numbers describe the possibility/chance of the flow to develop the effect. The liquid is in the saturated state when the pressurizing medium (gas) is dissolved in the hydraulic medium in the maximal amount (Fig. 4).

In a closed container, initially pressurized to the pressure p_{ini} , the partial pressure of the gas is given by

$$p_p = \frac{V_{\text{gas}} \cdot p_{\text{ini}} + \alpha_v V_{\text{oil}} \cdot p_0}{V_{\text{gas}} + \alpha_v V_{\text{oil}}}, \quad (4)$$

where α_v is the so-called Bunsen solvability coefficient, a constant specific for a particular combination of the gas and the liquid. Quantities V_{gas} and V_{oil} describe the geometry of the reservoir and are the gas chamber's volume and the

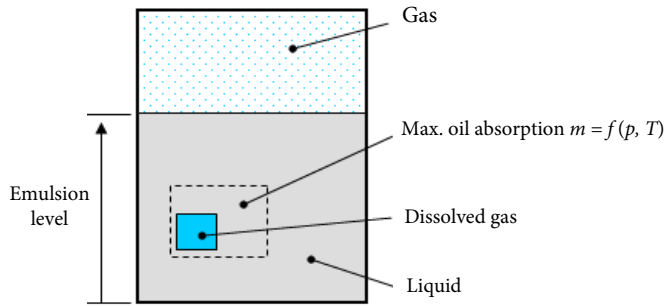


FIG. 4. Schematic illustration of the liquid aeration process.

total oil volume, respectively. Pressure p_0 is the atmospheric pressure and corresponds to the pressure during the storage of the liquid.

One notices the analogy between both phenomena and the dependence on the local pressure inside the flow. The noticeable difference is that the cavitation depends on the flow and intrinsic parameters of the hydraulic medium. By contrast, the aeration not only depends on the flow and physicochemical properties of both the hydraulic and the gas pneumatic media but also on the properties of the reservoir or the geometry of the entire device.

The continuous time-space formulation given in Eqs. (5)–(9) yields a much more computable description allowing quantification of the aeration effect influence on fluid parameters such as density and viscosity (see [30]). Aeration and cavitation are much more complex phenomena than they might appear from the description above. The magnitude of their effect depends on numerous factors: those immediately noticeable in Eqs. (2) and (3) or Henry’s law (5), but also elusive ones such as the purity of the liquid, sharpness of solid edges and the rate at which the stress is being applied to the liquid. Regarding the effect of aeration only, one is to consider the linear Henry’s equation, often known as “Henry’s law”

$$m = c_{GA}p_GV_l, \tag{5}$$

where m is the mass of the gas in the liquid, c_{GA} is the absorption coefficient, V_l is the volume of the liquid, and p_G is the partial pressure of the particular gas above the liquid. The absorption coefficient is often expressed by its reciprocal, called Henry’s coefficient. The content of gas bubbles in the liquid is equal to the difference between the initial partial gas pressure and local ones, and the following formula for the mass of gas in bubbles is derived:

$$m_{\text{gas}}(t) = m_{\text{ini}} - m(t) = c_{GA}(p_G^{\text{ini}} - p_G(t))\Delta V_l. \tag{6}$$

The quantity m_{ini} is the initial mass of gas dissolved in a given oil volume (hydraulic reservoir), p_G^{ini} is the initial pressure of the pressurizing medium, and

ΔV_l is the change in the volume of the liquid due to piston-rod operation (i.e., rebound or compression stroke). Computationally, in each numerical mesh cell of a finite element method of the volume $\Delta V_l(i)$ enumerated by i , the mass of gas in bubbles is

$$m_{\text{gas}}(t; i) = m_{\text{ini}} - m(t; i) = c_{GA}(p_G^{\text{ini}} - p_G(t; i))\Delta V_l(i). \quad (7)$$

Now, from the definition of the parameter χ in Eq. (1), the gaseous mass fraction, which is the mass of the free and the dissolved gas to the total mass of the fluid (the emulsion) in the shock absorber reservoirs, the time-dependence of the simulated value of χ given by

$$\chi(t) = 1 - \frac{m_{\text{oil}}}{m_{\text{oil}} + \sum_i m_{\text{gas}}(t; i)}. \quad (8)$$

Experimental observation of changes in the parameter $\chi(t)$ (see Fig. 3) was firstly reported in [30]. The transparent tube allowed to measure the height of the oil in the reserve tube during dynamic tests. Based on the geometry of the testing transparent unit (computed in CAD software, see Fig. 2), the actual volume of the emulsion was calculated, and from the temperature data, the theoretical pure oil volume could be found. The volume of gas in bubbles is the difference between the total volume of the emulsion and the theoretical volume of oil at a given temperature, as follows:

$$\chi = \frac{m_{\text{gas}}}{m_{\text{emulsion}}} = \frac{p_G V_G}{R_N T m_{\text{oil}} + p_G V_G}, \quad (9)$$

where T [K] is the temperature and P_G [Pa] is the absolute pressure and R [J/(kg · K)] is the specific gas constant, which for nitrogen is $R_N = 296.80$ [J/kg · K]. Figure 3 shows an evolution of the parameter χ averaged over a sequence of two tests performed on the transparent twin-tube shock absorber.

The risk that a particular valve design will cause aeration effects to occur may be assessed by evaluating a certain indicator based on post-processing CFD simulation data. In order to obtain a reliable ranking, the simulation (CFD) model has to be validated. The complete methodology encompasses the influence of the input design parameters, finite element model of the flow (CFD), analytical formulation of the UDFs (user-defined functions), image processing tools, and the experimental validation setup as well as visualization tools. The input design parameters are the reservoir volumes and their geometrical properties, valve type and its geometrical properties, physicochemical properties of the hydraulic liquid as well as such test conditions like the temperature. The single-phase model is a steady-state model that aims at predicting regions where gaseous fraction has a tendency to be concentrated, e.g., low-pressure regions at valve

outlet and its proximity and in the variable-volume reservoir (i.e., underpressure conditions due to rapidly increasing volume). Table 1 shows a qualitative comparison of the baseline experiment and different simulation methods, gradually simplifying the numerical simulation problem.

TABLE 1. The proposed quick-and-dirty method vs. complete evaluation using the multi-phase model.

	Experiment	Model			
Geometry	physical unit	3D	3D	3D	2D
Model	physical unit	FSI	CFD	CFD	CFD
Phases	physical unit	solid-gas-fluid	gas-fluid	fluid	fluid
Model parameters	N/A	distributed	distributed	distributed	distributed
Model dynamics	reference	steady-state (transient)	steady-state	steady-state	steady-state
Aeration measure	$\chi = \frac{m_{\text{gas}}}{m_{\text{emulsion}}} = \frac{m_{\text{gas}}}{m_{\text{gas}} + m_{\text{oil}}}$ cf. Eq. (1)/(9)			$\eta = \frac{\sum_i m_{\text{gas}}}{\sum_i m_{\text{gas}} + \sum_i m_{\text{oil}}}$ cf. Eq. (11)	
Simulation time	physical unit	days	hours	couple of minutes	minutes

The **risk of the aeration** is quantified using the parameter η representing the **local gas concentration indicator** (GCI) obtained for the local control volume (or area) represented by a grid of elementary cells covering the control volume. The cells involve a discrete division determined by the regular mesh, which interpolates the native single-phase steady-state CFD model mesh. The method flowchart is presented in Fig. 5.

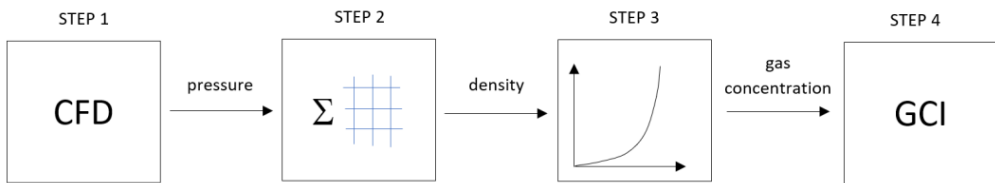


FIG. 5. The method flowchart.

The complete aeration risk assessment procedure consists of four essential steps:

STEP 1: Identify aeration risk regions in a shock absorber which are located near a sliding intake valve. Use a lamped-parameter twin-tube shock absorber model to identify a critical boundary pressure condition, i.e., maximum differential pressure based on input-output pressures to/from the control volume. Use the CFD model and conduct steady-state and single-phase flow simulations.

STEP 2: Extract pressure and velocity 2D/3D grid $[\mathbf{v}, \mathbf{p}] = f_{\text{CFD}}(\cdot)$ (see Eq. (10)).

STEP 3: Convert the pressure grid into a pressure density using a nonlinear pressure-density characteristic. The absolute distributed pressure functions $\rho_{\text{oil}}(\mathbf{p})$, gas $\rho_{\text{gas}}(\mathbf{p})$, and oil-gas emulsion $\rho_{\text{emu}}(\mathbf{p})$ are obtained using the predefined characteristics plotted in Fig. 6.

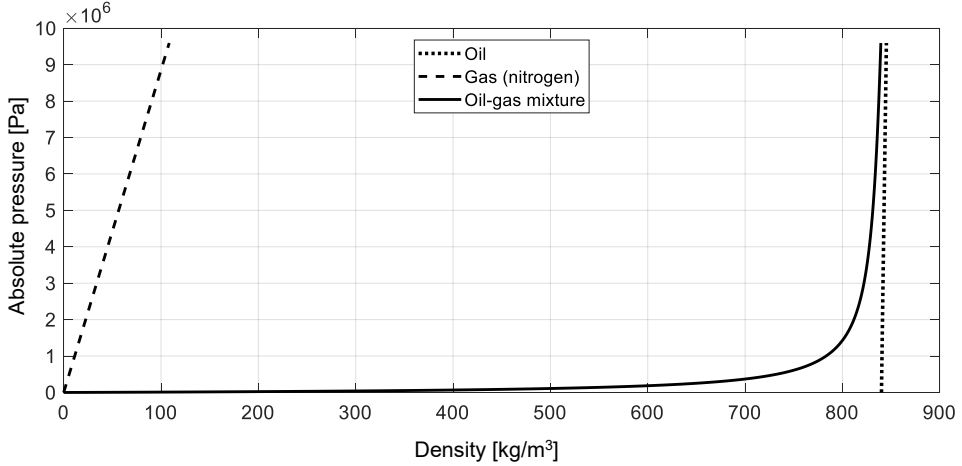


FIG. 6. Dependence of oil density on absolute pressure for oil $\rho_{\text{oil}}(\mathbf{p})$, gas $\rho_{\text{bubble}}(\mathbf{p})$, and oil-gas emulsion $\rho_{\text{emu}}(\mathbf{p})$.

STEP 4: Calculate gas concentration indicator $\eta = f_{\text{GCI}}(\cdot)$ (see Eq. (11)) in order to obtain gas/oil fractions, and finally, the parameter η for a uniformly distributed grid of cells with a resolution of 0.2 mm.

The complete aeration risk assessment procedure can be formalized using a set of nonlinear equations that have to be solved in order to obtain GCI represented by the parameter η in Eqs. (10) and (11). The set of equations for a steady-state single-phase CFD model is formulated as follows:

$$\left\{ \begin{array}{l} [\mathbf{v}, \mathbf{p}] = f_{\text{CFD}}(p_{\text{out}} - p_{\text{in}}), \\ \mathbf{m}_{\text{gas}} = \frac{x_0}{\rho_{\text{gas}}(\mathbf{p})} \cdot \frac{1}{\rho_{\text{emu}}(\mathbf{p})}, \\ \mathbf{m}_{\text{oil}} = \frac{1 - x_0}{\rho_{\text{fluid}}(\mathbf{p})} \cdot \frac{1}{\rho_{\text{emu}}(\mathbf{p})}, \\ \eta = f_{\text{GCI}}(\mathbf{m}_{\text{gas}}, \mathbf{m}_{\text{oil}}), \end{array} \right. \quad (10)$$

where f_{CFD} is the 2D/3D CFD simulation function, while \mathbf{v} , \mathbf{p} are two- or three-dimensional matrices of the fluid velocity, pressure, gas mass and fluid

mass, respectively, $p_{\text{out}} - p_{\text{in}}$ is the scalar differential pressure across the valve assembly, $x_0 = 1e^{-3}$ is the initial ratio of the gaseous mass fraction to the mass of the oil (usually x_0 is in the range $(1e^{-4}; 1e^{-7})$), the parameter η is the scalar gas concentration measure, and f_{GCI} is the function that allows to obtain the GCI for a representative area or volume of a shock absorber interior we have:

$$\eta = f_{\text{GCI}}(\mathbf{m}_{\text{gas}}, \mathbf{m}_{\text{oil}}) = \frac{\sum_i m_{\text{gas}}}{\sum_i m_{\text{gas}} + \sum_i m_{\text{oil}}}, \tag{11}$$

where m is the mass concentrated in the gas or fluid finite element, while i is the number of finite elements within the representative control area or volume for 2D and 3D models. The matrices \mathbf{p} and \mathbf{v} are interpolated uniform elements of the native CFD mesh with a specific resolution. The cells represent the average values of the reported parameters (pressure and velocity).

The proposed method requires a lumped parameter model of a shock absorber in order to obtain differential pressure, which is the boundary condition of the CFD model simulation (Fig. 6). It is also feasible to measure the differential pressure experimentally using transparent tooling (Sec. 5) for existing shock absorbers.

In order to obtain reliable CFD simulation results, the model has to be validated by means of an experimental approach. The results of numerical CFD simulations are compared with the results of the adequate experiment (Secs. 5 and 6). The most reasonable way of making such a comparison appears to be comparing the simulated and measured velocity fields. The velocity vector field is obtained as a result of the image post-processing by applying a technique called PIV (Sec. 6).

5. CFD MODEL

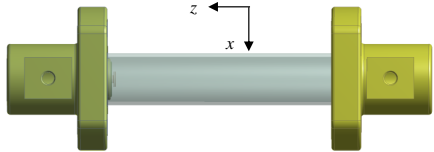
Mathematical models are used to define turbulence within CFD simulations, such as RANS, LES, DES and DNS [26]. Nevertheless, the RANS model is the most commercially accepted form of turbulence modeling due to an effective compromise between accuracy and computation time, where solving approaches include $k - \epsilon$, $k - \omega$, SAS, SST, RSM, and mixing length model, to name a few (Versteeg and Malalasekera [31], Xing *et al.* [34]). FSI simulations offer an encompassing model of damper valve physics, but the accuracy of these simulations, namely the CFD portion, is highly dependent on experimental validation from flow field analysis [31]. A detailed flow analysis of the valve can also provide additional information about fundamental valve dynamics during operation. For instance, Lee [21] identified that a cavitation influences the correlation accuracy and conclude that this cavitation effect has minimal effect on the damper's

hydraulic performance, which contradicts much of the literature. As a result, Lee [21] suggested that further study is necessary to predict the onset of cavitation, which is also confirmed by Rifai *et al.* [28], who acknowledged that pressure data around the valve is useful for examining the initiation of fluid cavitation.

There is a general agreement in the research literature that the fluid flow through the damper valve is the least understood yet most crucial flow within the damper, where the flow rate is proportional to the valve deflection with complex interaction. For example, LaJoie [19] recognized that the valve disk has the most critical resistance coefficient, where the fluid forces acting on the disk are a function of fluid impulse pressure, fluid dynamic pressure and valve pressure differential. Fluid impulse is the result of fluid stagnation pressure generated from a change in flow direction as the fluid strikes the valve structure. The fluid dynamic pressure is the result of viscous flow losses generated as fluid flows around the valve structure. The valve pressure differential is simply the difference in pressure acting upon each side of the deformable valve structure. Duym *et al.* [14] and many other authors opted to neglect the impulse effects from the equations that couple valve deflection with fluid flow and at low excitation velocities both the inertial and viscous effects were neglected. Kasteel *et al.* [17] identified that these coupling equations between valve deflection and flow are dependent on the valve deflection, where viscous forces dominate inertial (impulse) forces at small deflections and vice versa at large deflections.

The CFD model was used in order to reproduce the experimental setup conditions in all the required details. It is assumed that there is an incompressible flow model, $k - \omega$ wall model and 3D partial symmetrical model. The model geometry simplification process is shown in Table 2.

TABLE 2. The model geometry simplification process.

Model geometry	Description
	Step 1: The external tooling mechanical components (i.e., hydraulic fittings) and valve minor components (i.e., the valve coil spring, the other valve washers) were removed
	Step 2: The fluid domain was extracted and modeled removing all solid elements
	Step 3: The geometry was reduced to the boundary conditions indicated by the gray frame
 0.95 [bar] 0.35 [bar]	Step 4: The boundary inlet-outlet pressure conditions were applied

The model incorporates a three-dimensional (3D) non-axisymmetrical geometrical discretization with a finite element mesh (Figs. 8–11). The mesh summary is presented in Table 3.

TABLE 3. The CFD model mesh summary.

Mesh parameters	Values
Number of nodes	2 374 229
Number of elements	9 336 750
Minimum element size	6.505393e-03
Maximum element size	0.99999
Average element size	0.71213
Standard deviation element size	0.25892

The geometry was meshed in a manner in which a balance between the accuracy and the numerical effort was achieved involving 9.3 million elements, where linear tetrahedral elements (NASTRAN element name is CTETRA [25]) dominate (Fig. 7).

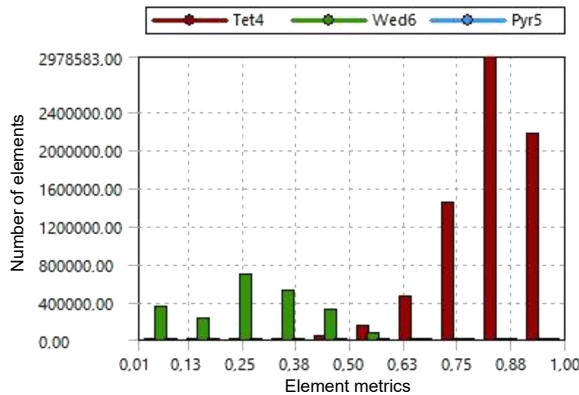


FIG. 7. The mesh type of elements. Pareto chart (Tet4 – four-node linear tetrahedral element, Wed6 – six-node linear wedge element, Pyr5 – five-node linear pyramid element).

The side-wall mesh includes five finite elements (Figs. 8–11).

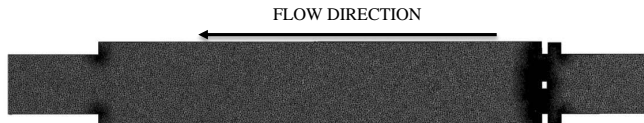


FIG. 8. The total meshed flow volume.

Taking into consideration the irregularities of the flow path passing through the valve cavity, the turbulent flow model turned out to be the most appropriate;

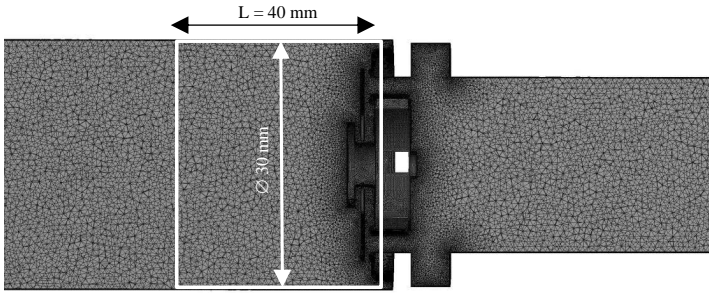


FIG. 9. The part of the total meshed flow volume below and above the shim sliding valve.

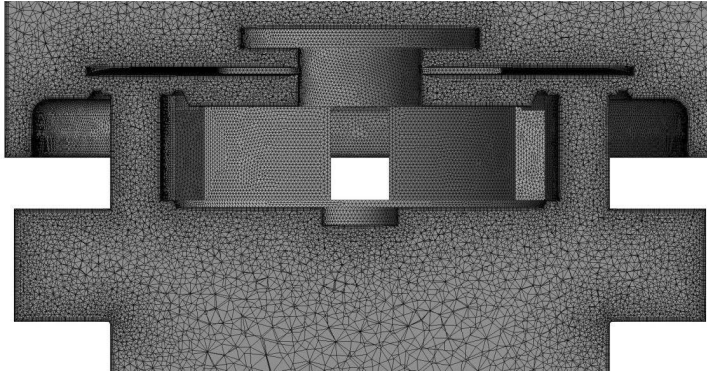


FIG. 10. The mesh visualization (enlarged view on the valve).

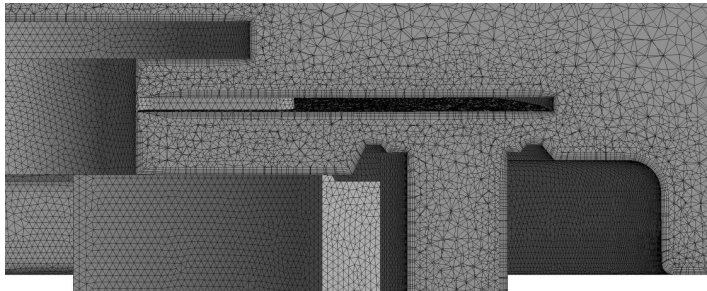


FIG. 11. The mesh visualization (enlarged symmetrical right part of Fig. 10 of the valve body and the sliding shim).

the shear stress transport (SST) model combining the $k-\epsilon$ and $k-\omega$ models was applied. The $k-\omega$ model ensures an accurate flow modeling in flow regions in close proximity to the channel walls, while the $k-\epsilon$ model ensures high accuracy in the strict interior of the channel [23]. The convergence criteria for the solver (iteration-stop criteria) were selected to be equal to $\epsilon = 10^{-4}$ for the residual or $n = 100$ iterations. The properties of the hydraulic fluid are listed in Table 4.

TABLE 4. Fluid properties used in the flow simulation.

Parameters	Units	Values
Density	kg/m ³	800
Dynamic viscosity	mPa·s	40
Working pressure range	MPa	0–20
Thermal expansion coefficient	%/°C	0.1
Viscosity indicator	%/°C	–2
Viscosity-pressure sensitivity	%/MPa	+3
Compressibility	%/MPa	+0.04
Specific thermal capacity	kJ/kg·K	2.5

Figure 12 shows the CFD simulation results in the form of the projection of the velocity vectors on a selected plane. The plane contains the axis of the symmetry of the flow geometry and the cross-section through the valve body channels – the flow structures are symmetrical. Similarly, another type of flow visualization, the scalar velocity field, shown in the bottom pane, shows similar symmetry based on a cross-section not containing valve body channels.

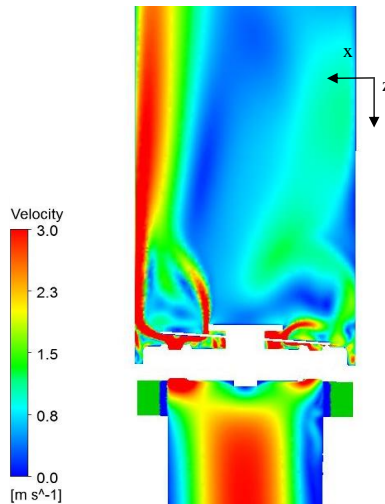


FIG. 12. CFD simulation results shown as the projected vectors of the velocity field on a cross-section passing through valve channels.

6. PIV EXPERIMENTAL SETUP

The PIV technique is the most recent development in optical methods for non-invasive flow measurement. The fundamental idea of this measurement technique is straightforward. The flow of interest is seeded with small tracer particles,

and then their images are recorded with a digital camera. The fluid velocity field is determined by finding displacements of tracer particles between two subsequent images if the time lag between them is known. The complete measurement setup and procedure are presented by Czop *et al.* [6].

An experimental setup [9] was designed and built for the purpose of PIV measurements of the flow through an intake valve assembly reproducing shock absorber operational conditions. The base valve assembly (Figs. 13 and 14) under investigation is mounted into transparent tooling equipped with a polycarbonate pipe allowing the flow through the valve to be observed.

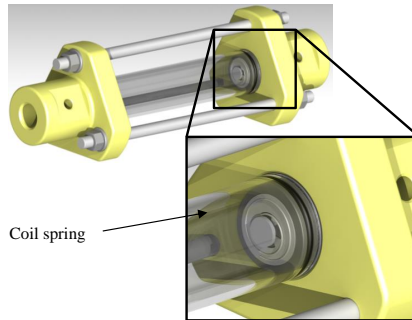


FIG. 13. Transparent valve casing and valve magnification showing a top-view of the valve.

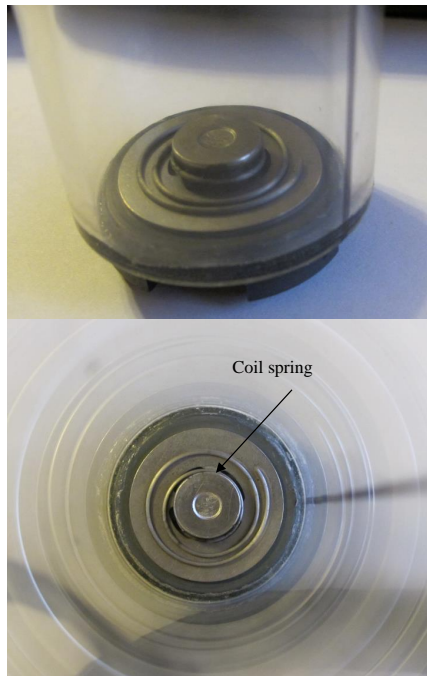


FIG. 14. The valve inside the transparent casing.

The flow is directed in such a manner that it lifts the sliding shim supported by the coil spring (Fig. 14). The full-open washer position is assumed for CFD simulation work.

The hydraulic circuit and its schematic representation are presented in Fig. 15, including the hydraulic supply device, hydraulic lines, pressure sensor, and tested valve placed in the transparent tube. The MTS 858 servo-hydraulic test rig was

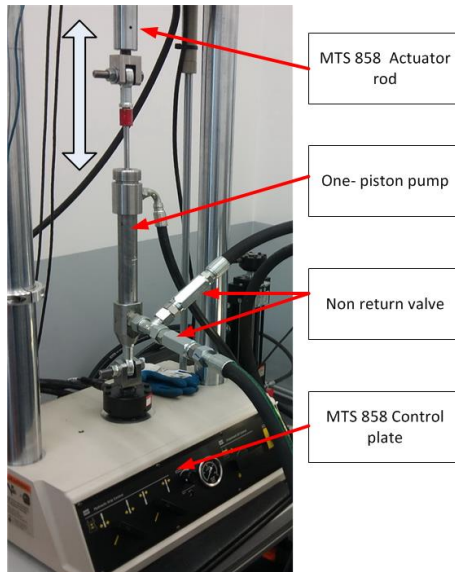
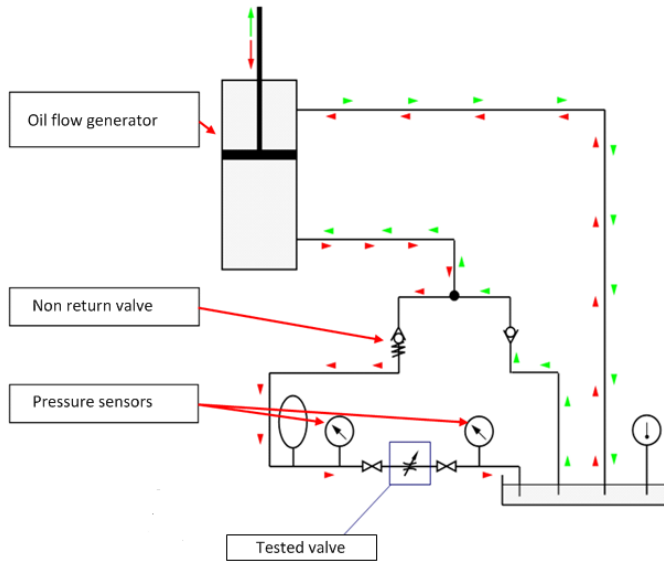


FIG. 15. Schematic representation (top view) and photo (bottom view) of the experimental hydraulic setup.

used to force the hydraulic cylinder (i.e., oil flow generator) to ensure the desired mass-flow rate of the flow through the valve. The hydraulic installation allows to supply the differential pressure over the tested valve using specific hydraulic one-way valves and simulate the shock absorber compression and rebound stroke conditions. The green arrows indicate the rebound stroke, while the red arrows indicate the compression stroke and corresponding flow and movement of the piston-rod of the oil flow generator forced through the rod of the MTS 858 test rig (Fig. 15).

The entire equipment was designed in a manner to allow an image of the velocity field of the flow's liquid phase to be taken using digital PIV (Fig. 16).

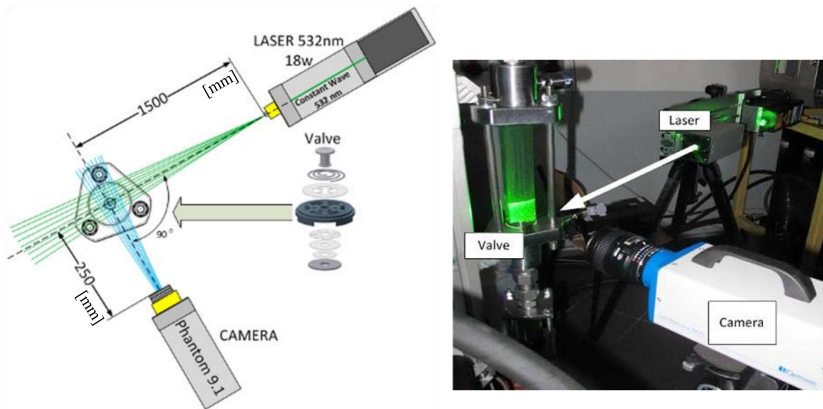


FIG. 16. Particle imaging velocimetry (PIV) 2D setup schematic (left) and photo of the actual installation (right).

The PIV system used in measurements consisted of a high-speed Phantom v9.1 digital camera set to 1016 FPS and a resolution of 1632×1200 pixels with a 14-bit image depth. The camera was equipped with a high-quality Nikon lens with a 50 mm focal length. A high-power green (532 nm) CW DPSS (continuous wave diode-pumped solid state) laser was used to illuminate the flow. The gathered images were processed using the Matlab software package. The velocity vectors were calculated using the hierarchical cross-correlation method. In this approach, vectors are calculated iteratively, starting with a large interrogation window and gradually the window size is decreased with subsequent iterations of the algorithm. The initial window size equal to 64×64 was used and five iterations of the algorithm were carried out with the final window size equal to 16×16 pixels. At each iteration, the displacement map was estimated with the cross-correlation function. The seeding particles were ceramic dust with a $0.1 \mu\text{m}$ mean diameter.

The valve was supplied with pressure using an injector based on the servo-hydraulic tester, as discussed in [6]. The inlet-outlet pressure was captured using

the pressure sensors installed at the inlet and outlet hydraulic lines to the transparent tube (Fig. 17).

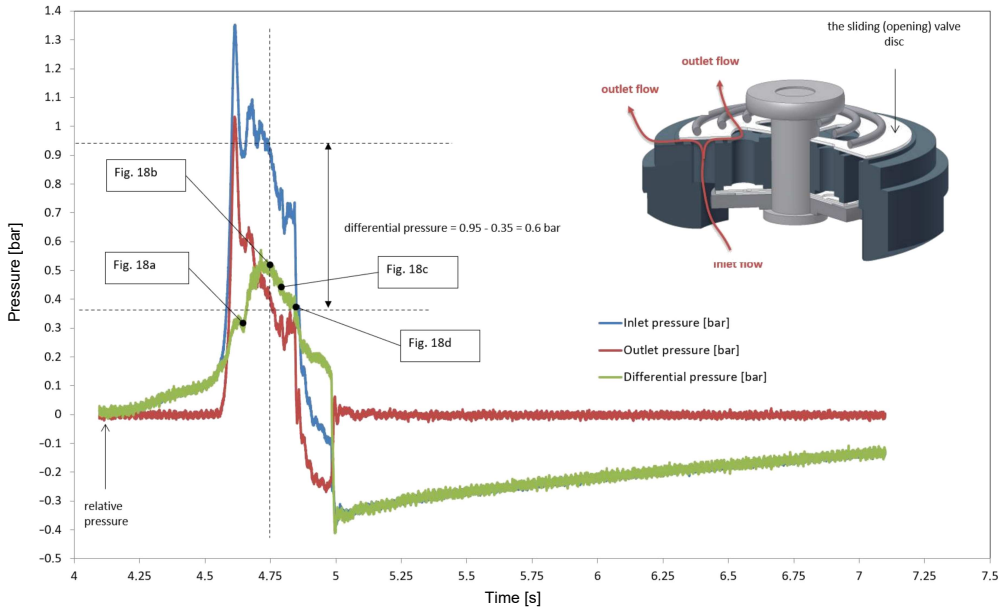


FIG. 17. The inlet-outlet pressure measurement data in the function of time.

7. CFD MODEL VALIDATION RESULTS

The CFD model validation was performed using the PIV experimental setup introduced in Sec. 6. A triangle wave signal of 80 mm stroke @ 1 m/s velocity was used to build the pressure that opens the valve (compression direction). The valve opens in an asymmetrical mode primarily due to the coil spring asymmetry, with its end-support position not controlled during the assembling process. The valve opening-closing phases are visualized in Fig. 18 with seeding particles in the background.

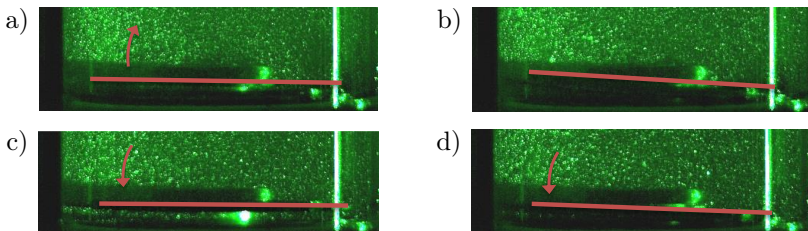


FIG. 18. The valve opening-closing phases according to: a) opening phase around $T = 4.65$ s, b) max. opening around $T = 4.75$ s, c) closing phase around $T = 4.8$ s, d) closing phase around $T = 4.85$ s.

The valve opening moment is shown in Fig. 19 without the seeding particles.



FIG. 19. A valve opening moment captured by a camera at $T = 4.75$ s, as shown in Fig. 18b.

Figure 20 shows exemplary images generated by the PIV technique. The left image (Fig. 20a) is a raw image from the charge-coupled device (CCD) camera with red boxes indicating examples of unwanted reflections from an external light source. The magnification shown in the bottom-right image (Fig. 20b) is used to indicate the baseline of the measurement area (yellow line) above the valve assembly. The measurement area is restricted by the calibration plate with a grid bounded by A-B-C-D points and defined by the capture image of a high-speed PIV camera. The same boundary is shown on the PIV processing result – a velocity (scalar) map computed by the PIV processing algorithms described in Sec. 6. Tracer particles and the plane of the light sheet are clearly visible.

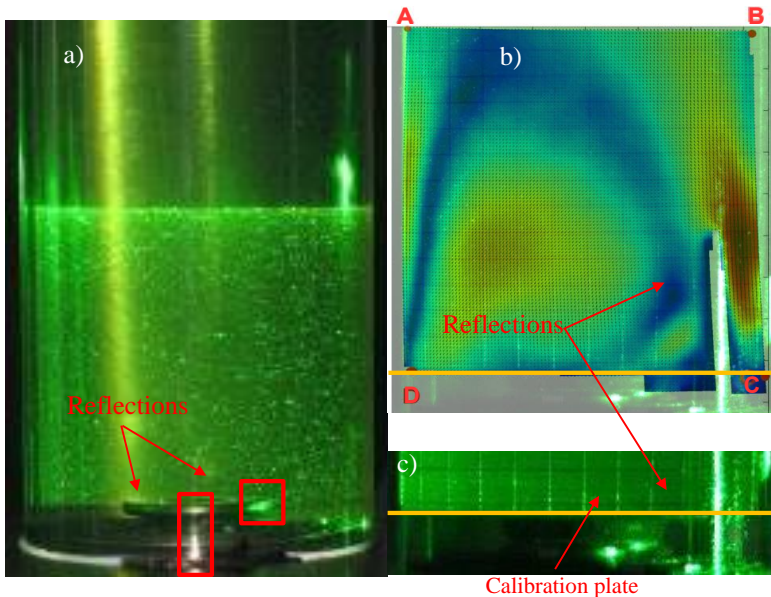


FIG. 20. a) A direct image from the CCD camera used in the PIV setup, b) the base-line of the flow in the capturing images (yellow line) and c) a screen-shot of the scalar velocity field computed from the PIV measurements, red rectangles denote unwanted glass reflections, A-B-C-D points determine the measurement area based on the calibration plate.

Figure 21 shows the final results of image processing, namely the velocity map (the z -axis is calibrated in m/s), and compares the flow structures between the PIV processor and the post-processing algorithms extracting the velocity field from the CFD-simulated vector field section.

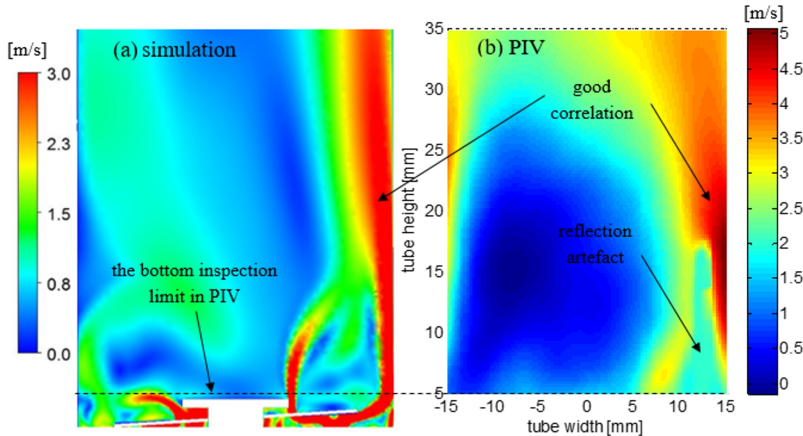


FIG. 21. Comparison of the velocity image obtained by a) CFD simulation and b) PIV method; the velocity range is similar in both images and defined by the color bar.

A moderate correlation between low-velocity areas in the center of the CFD and PIV images is observed. A good agreement is observed between high-velocity jet areas (to the right side of both images). The agreement between the two images is not as expected in the remaining area. The discrepancy may be attributable to glare from the casing's exterior surface, as well as to possible instrumentation misalignment and the refraction effect on the thick glass wall (> 10 mm).

The work described in this section proves the method to be feasible and capable of providing data useful in validating CFD and FSI simulation models. Post-processing has been created to extract appropriate mesh elements, their volumes, as well as pressure values and velocity vector coordinates, and to compute projections onto a plane defined in the PIV physical experiments by the sheet of light. Visualization algorithms were also created. Nevertheless, the reported accuracy does not ensure complete quantitative agreement between the CFD and PIV.

8. THE METHOD APPLIED TO EVALUATE AERATION RISK

The valve geometry is a significant contributor causing increases in the speed of the fluid aeration effect or inducing the cavitation phenomenon. The fluid velocity measurements are required to adjust the simulation CFD model appli-

cable to valve system design and early detection of any aeration/cavitation risk occurrence [5].

The developed aeration risk-assessing method was experimentally demonstrated based on the control area in the experimental patented fixture [9], which is equivalent to a twin-tube shock absorber. The fixture is described in Sec. 5. The control volume is indicated in Table 2 by a gray frame (Step 3) and its 3D view is shown in Fig. 22. The meshed control volume is visualized in Figs. 8–11 and bounded by a gray frame including basic dimensions. The control volume was further reduced to a control area, as shown in Fig. 22. The cross-section is symmetrically over the flow passages.

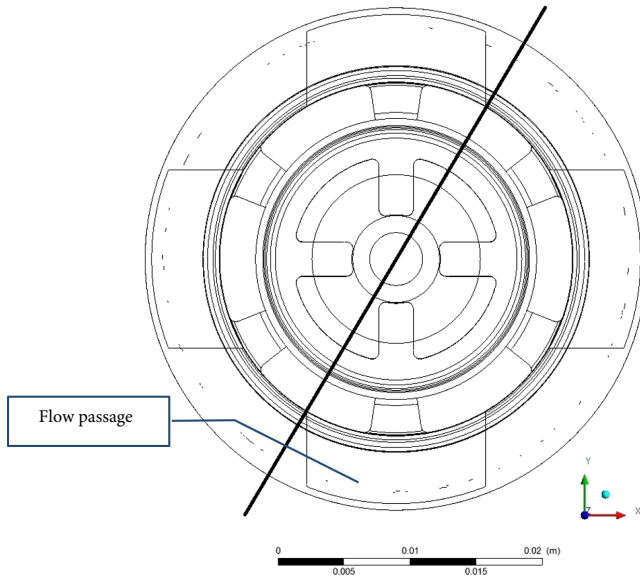


FIG. 22. Control volume reduced to a control area, the experimental tube cross-section surface bounded by the internal tube diameter (see Figs. 16–19).

The native CFD mesh cells have a density of 0.1–1 cells/mm. In this study, the CFD pressure field map was converted into a uniformly discretized field consisting of an elementary cell of finite elements of the size 0.2 mm. Figure 23 shows schematically the squared centers of obtained finite elements and the assigned interpolated pressure values belonging to each square center by means of a color range. The gas and oil concentration maps were adequately obtained.

The obtained gas fraction is visualized on a colored map of finite elements in Fig. 7. The aeration risk measure is calculated according to Eq. (11):

$$\eta = f_{GCI}(\mathbf{m}_{\text{gas}}, \mathbf{m}_{\text{oil}}) = \frac{\sum_i m_{\text{gas}}}{\sum_i m_{\text{gas}} + \sum_i m_{\text{oil}}} = 0.0051 = 5.1e^{-3}.$$

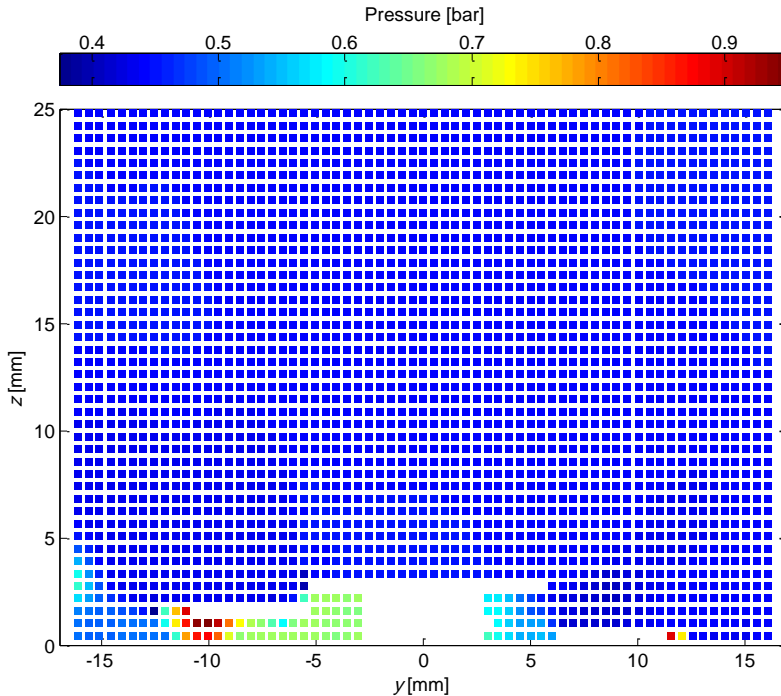


FIG. 23. A reference finite element pressure map values uniformly discretized over the representative volume.

Some statistics can be included taking into account the greater gas content over all finite squares and finding the maximum value of the matrix \mathbf{m}_{gas} , i.e., $\max\{\mathbf{m}_{\text{gas}}\}$.

9. SUMMARY

Leading shock absorber manufacturers are implementing innovative analytical methods to eliminate operational issues, such as uncontrolled vibrations and variability of damping force characteristics in operation, to provide vehicle manufacturers with high-quality shock absorbers. The presence of the free gas (bubbles) increases the compressibility of the working medium in the shock absorber reservoirs, thus causing a measurable so-called aeration effect, which has a negative low- and high-frequency impact on a shock absorber performance. The shock absorber engineering and manufacturing process requires a quick-and-dirty approach in order to evaluate a couple of valve settings every day without extensive and time-consuming laboratory tests. The major contributor to negative aeration effects is the sliding intake valve that passes the hydraulic medium previously exposed to a soluble gas in the reserve tube. The valve geometry causes

local pressure drop regions and, consequently, the risk of releasing the dissolved gas in the passing fluid. The aeration effect can be experimentally quantified and measured based on the parameter χ that can be only calculated in a case of a transparent shock absorber.

Nevertheless, the proposed quick-and-dirty method allows to evaluate regular shock absorbers in the production or design stage using a simulation approach. The method belongs to the class of the ranking and selection methods, which is a group of analytical and statistical techniques used to justify selecting the best among a finite set of alternatives. Selection of the best alternative is made according to an ordering of alternatives according to the estimation of a selected measure. The focal point here is the development and validation of the valve design alternatives ordering with respect to the expected average bubble content in the predefined volume of the hydraulic liquid known to be attributable to the aeration effect. Such a ranking measure is called the aeration ‘risk’. The aeration risk measure is to give the simulated, averaged ratio of the gas content of bubbles entrained in the liquid to the sum of the mass of entrained bubbles to the mass of the hydraulic medium. Aeration risk is assessed by ranking the model predictions expressed in terms of the mixture’s gaseous to fluid mass fractions of according to the GCI.

GCI proposed and discussed in this paper is a synthetic measure of aeration risk phenomena occurrence, allowing underperforming shock absorber valve settings to be evaluated and rejected. GCI calculation requires a calibrated CFD model of a shock absorber’s arbitrary selected intake-valve hydraulic region and the supporting lumped-parameter model in order to provide boundary flow conditions for the CFD model. The paper not only focused on the proposed method but also discussed the process of PIV experiments to validate a CFD model, which is part of the analytical tools used in the method. The paper reports experimental PIV measurements in order to determine a velocity map of the flow developed across a shim sliding relief valve. The velocity map is required to validate and adjust the CFD model based on experimental data to correctly obtain the pressure drop map along the valve geometry. The experiment was carried out using the patented fixture [9], which is capable of emulating all the working principles of a common sliding shim relief valve used in shock absorbers. CFD post-processing was applied to extract appropriate mesh elements, their volumes, as well as velocity vector coordinates and to compute projections onto a plane defined in the PIV physical experiments by the sheet of light. CFD simulation of the phenomenon is demonstrated to moderately agree with measurements. Further tests were not possible within the research project.

The method was applied in engineering practice as similar shock absorber designs were considered to be ranked regarding gas concentration indicator. The comparable application conditions (i.e., similar sliding valve differing only in

geometrical features, the same cylinder diameter and GCI calculation regions) resulted in good performance of the aeration risk assessment method. The general recommendation is that 2D GCI is applicable in assessing the risk of aeration occurrence for axisymmetrical sliding intake valves, while 3D GCI should be applied in all other cases.

Through a feasibility study, this work demonstrates that the proposed method intended to optimize the disc-relief valves is applicable in the automotive industry. The methodology is constructed based on three ‘pillars’: simulation, experimental validation and data processing. Simulation is necessary to obtain insight into the system’s internal states that are otherwise not available to any direct measurement method. The approach of utilizing a single-phase CFD model in order to identify sub-volumes of the flow that have a tendency to generate the aeration or cavitation effects, or both, is applicable to the pre-development phase of a valve system design process and aims at eliminating the weakest designs in terms of the risk of occurrence of the aeration/cavitation effects. However, such an approach does not aim to predict the absolute magnitude of the aeration effects that will eventually be observed for a given design. Due to the level of complication of the simulation problem, unknown magnitudes of errors in estimated initial and boundary conditions, as well as potential deficiencies in the simulation model and data processing algorithms, attempt to extensively validate the CFD model using a DOE approach would be premature and needs further study.

FUNDING

This work was supported by the Polish Ministry of Science (MNiI) [research project N504 494239].

REFERENCES

1. M. Alonso, Á. Comas, Modelling a twin tube cavitating shock absorber, *Proceedings of the Institution of Mechanical Engineers, Part D: Journal of Automobile Engineering*, **220**(8): 1031–1040, 2006, doi: 10.1243/09544070D23104.
2. C.E. Brennen, *Cavitation and Bubble Dynamics*, Cambridge University Press, 2014.
3. G. Cavazzini [Ed.], *The Particle Image Velocimetry: Characteristics, Limits and Possible Applications*, InTechOpen, London, 2012.
4. S.L. Ceccio, C.E. Brennen, Observations of the dynamics and acoustics of travelling bubble cavitation, *Journal of Fluid Mechanics*, **233**: 633–660, 1991, doi: 10.1017/S0022112091000630.

5. P. Czop, J. Gniłka, Reducing aeration and cavitation effect in shock absorbers using fluid-structure interaction simulation, *Computer Assisted Methods in Engineering and Science*, **23**(4): 171–189, 2016, <https://comes.ippt.pan.pl/index.php/comes/article/view/181>.
6. P. Czop, M. Hetmańczyk, G. Wszolek, J. Słoniewski, D. Gąsiorek, Z. Buliński, Particle image velocimetry technique applied to flow evaluation through a shock absorber intake valve, [in:] *4th International Conference Mechatronics: Ideas for Industrial Applications*, September 13–15, Gliwice, Wisła-Jawornik, Poland, pp. 38–39, 2017.
7. P. Czop, D. Sławik, A high-frequency first-principle model of a shock absorber and servo-hydraulic tester, *Mechanical Systems and Signal Processing*, **25**(6): 1937–1955, 2011, doi: 10.1016/j.ymssp.2011.01.011.
8. P. Czop, D. Sławik, T. Włodarczyk, M. Wojtyczka, G. Wszolek, Six Sigma methodology applied to minimizing damping lag in hydraulic shock absorbers, *Journal of Achievements in Materials and Manufacturing Engineering*, **49**(2): 243–250, 2011.
9. P. Czop, G. Wszolek, M. Hetmańczyk, J. Dawid, *A device to determine the parameters of passive valve operation, particularly disc valves of hydraulic dampers, using PIV method* (granted patent), Silesian University, PL407553; PL222810, 2015.
10. P. Czop, G. Wszolek, M.P. Hetmańczyk, The effects of the aeration phenomenon on the performance of hydraulic shock absorbers, [in:] A. Mężyk, S. Kciuk, R. Szewczyk, S. Duda [Eds.], *Modelling in Engineering 2020: Applied Mechanics. SMWM 2020. Advances in Intelligent Systems and Computing*, vol 1336, Cham, Springer, 2020, doi: 10.1007/978-3-030-68455-6_2.
11. R. Andrighetto, Dynamic and thermal model for hydraulic shock absorbers, PhD Thesis, Politecnico di Torino, 2018.
12. N.G. Deen, J. Westerweel, E. Delnoij, Two-phase PIV in bubbly flows: status and trends, *Chemical Engineering & Technology*, **25**(1): 97–101, 2002, doi: 10.1002/1521-4125(200201)25:1<97::AID-CEAT97>3.0.CO;2-7.
13. J. Dixon, *The Shock Absorber Handbook*, John Wiley & Sons, 2007.
14. S. Duym, R. Stiens, K. Reybrouck, Evaluation of shock absorber models, *Vehicle System Dynamics*, **27**(2): 109–127, 1997, doi: 10.1080/00423119708969325.
15. S.W. Duym, R. Stiens, G. Baron, K. Reybrouck, *Physical modeling of the hysteretic behaviour of automotive shock absorbers*, SAE Technical Paper No. 970101, Society of Automotive Engineers, 1997, doi: 10.4271/970101.
16. C.O. Iyer, W.-J. Yang, *Analysis on liquid-vapor bubbly-flow systems in reciprocating motion*, *Journal of Fluids Engineering*, **121**(1): 185–190, 1999, doi: 10.1115/1.2822000.
17. R. Van Kasteel, C.-G. Wang, L. Qian, J.-Z. Liu, G.-H. Ye, A new shock absorber model for use in vehicle dynamics studies, *Vehicle System Dynamics*, **43**(9): 613–631, 2005, doi: 10.1080/0042311042000266720.
18. B. Koren, P.F.M. Michielsen, J.-W. Kars, P. Wesseling, A computational method for high-frequency oleodynamics: application to hydraulic-shock-absorber designs, *Surveys on Mathematics for Industry*, **7**: 283–301, 1998.

19. J.C. LaJoie, *Damper Performance Development*, SAE Technical Paper No. 962551, Society of Automotive Engineers, 1996, doi: 10.4271/962551.
20. J.L. Lebowitz, O. Penrose, Modern ergodic theory, *Physics Today*, **26**(2): 23–29, 1973.
21. K. Lee, Numerical modelling for the hydraulic performance prediction of automotive monotube dampers, *Vehicle System Dynamics*, **28**(1): 25–39, 1997, doi: 10.1080/00423119708969347.
22. F. Luo, X.L. Zhang, A review of aeration and cavitation phenomena in the hydraulic shock absorber, [in:] *Advances in Mechatronics, Robotics and Automation II*, Trans Tech Publications, Ltd, vol. 536–537, pp. 1369–1373, 2014, doi: 10.4028/www.scientific.net/amm.536-537.1369.
23. F. Menter, Zonal two equation $k - \omega$ turbulence models for aerodynamic flows, [in:] *23rd Fluid Dynamics, Plasmadynamics, and Lasers Conference*, AIAA-93-2906, 1993, doi: 10.2514/6.1993-2906.
24. G. Morettini, N. Bartolini, D. Astolfi, L. Scappaticci, M. Becchetti, F. Castellani, Experimental diagnosis of cavitation for a hydraulic monotube shock absorber, *Diagnostyka*, **17**(3): 75–80, 2016.
25. MSC.Software Corporation, *MSC.Nastran 2001. Getting Started with MSC.Nastran. User's Guide*, MSC Software Corporation, Santa Ana, CA, 2000, www.ae.metu.edu.tr/~ae464/getstart.pdf.
26. S.V. Patankar, *Numerical Heat Transfer and Fluid Flow*, CRC Press, Boca Raton, 2018.
27. M. Raffel, C.E. Willert, F. Scarano, C.J. Kähler, S.T. Wereley, J. Kompenhans, *Particle Image Velocimetry: A Practical Guide*, Springer, 2013.
28. S.M. Rifai, J.C. Buell, Z. Johan, J.A. Landers, A.B. Glendinning, J.A. Landers, *Automotive engineering Applications of Multiphysics Simulation*, SAE Technical Paper 1999-01-1022, Society of Automotive Engineers, 1999, doi: 10.4271/1999-01-1022.
29. F. Martins, C. Siqueira, N. Spogis, *Development and validation of a CFD model to investigate the oil flow in a shock absorber*, SAE Technical Paper 2005-01-4030, 2005, doi: 10.4271/2005-01-4030.
30. D. Sławik, P. Czop, A. Król, G. Wszolek, Optimization of hydraulic dampers with the use of Design For Six Sigma methodology, *Journal of Achievements in Materials and Manufacturing Engineering*, **43**(2): 676–683, 2010.
31. H.K. Versteeg, W. Malalasekera, *An Introduction to Computational Fluid Dynamics: The Finite Volume Method*, Pearson Education, 2007.
32. G. Del Vescovo, A. Lippolis, S. Camporeale, *Investigation of the flow field inside fluid power directional control valves by means of particle image velocimetry*, [in:] *Atti Del XIV Convegno Nazionale Aivela-Roma*, November 6–7, 2006.
33. T.H. Włodarczyk, P. Czop, D. Sławik, G. Wszolek, Automatic shape identification by data-driven algorithms with applications to design optimizing in hydraulics, *Journal of Transdisciplinary Systems Science*, **16**(1): 35–43, 2012.

34. T. Xing, J. Shao, F. Stern, BKW-RS-DES of unsteady vortical flow for KVLCC2 at large drift angles, [in:] *Proceedings of the 9th International Conference on Numerical Ship Hydrodynamics*, Ann Arbor, Michigan, August 5–8, 19 pages, 2007.
35. F. Herr, T. Mallin, J. Lane, S. Roth, *A Shock Absorber Model Using CFD Analysis and Easy5*, SAE Technical Paper 1999-01-1322, 1999, doi: 10.4271/1999-01-1322.
36. M. Shams, R. Ebrahimi, A. Raoufi, B.J. Jafari, CFD-FEA analysis of hydraulic shock absorber valve behavior, *International Journal of Automotive Technology*, **8**(5): 615–622, 2007.
37. S.S. Kulkarni, B. Ravi, M. Magdum, A Nonlinear Contact Analysis of An Automotive Shock Absorber Shims Using Fluid Structure Interaction Technique, [in:] Altair Technology Conference, India, 2013.
38. F.G. Guzzomi, P. O’neill, A. Tavner, *Investigation of Damper Valve Dynamics Using Parametric Numerical Methods*, [in:] 16th Australasian Fluid Mechanics Conference Crown Plaza, Gold Coast, Australia, December 2–7, 2007.

*Received April 21, 2021; revised version March 27, 2022;
accepted June 21, 2022.*